The Astrophysical Journal, 937:13 (11pp), 2022 September 20 https://doi.org/10.3847/1538-4357/ac87ff

Photometrically Classified Superluminous Supernovae from the Pan-STARRS1 Medium Deep Survey: A Case Study for Science with Machine-learning-based Classification

Brian Hsu[1], Griffin Hosseinzadeh[2], V. Ashley Villar[3,4,5], and Edo Berger[1,6]
[1] Center for Astrophysics | Harvard & Smithsonian, 60 Garden Street, Cambridge, MA 02138-1516, USA; brianhsu@college.harvard.edu
[2] Steward Observatory, University of Arizona, 933 North Cherry Avenue, Tucson, AZ 85721-0065, USA
[3] Department of Astronomy & Astrophysics, The Pennsylvania State University, University Park, PA 16802, USA
[4] Institute for Computational & Data Sciences, The Pennsylvania State University, University Park, PA 16802, USA
[5] Institute for Gravitation and the Cosmos, The Pennsylvania State University, University Park, PA 16802, USA
[6] The NSF AI Institute for Artificial Intelligence and Fundamental Interactions, USA
Received 2022 April 20; revised 2022 July 27; accepted 2022 August 7; published 2022 September 16

Abstract

With the upcoming Vera C. Rubin Observatory Legacy Survey of Space and Time (LSST), it is expected that only ∼0.1% of all transients will be classified spectroscopically. To conduct studies of rare transients, such as Type I superluminous supernovae (SLSNe), we must instead rely on photometric classification. In this vein, here we carry out a pilot study of SLSNe from the Pan-STARRS1 Medium Deep Survey (PS1-MDS), classified photometrically with our `SuperRAENN` and `Superphot` algorithms. We first construct a subsample of the photometric sample using a list of simple selection metrics designed to minimize contamination and ensure sufficient data quality for modeling. We then fit the multiband light curves with a magnetar spin-down model using the Modular Open-Source Fitter for Transients (`MOSFiT`). Comparing the magnetar engine and ejecta parameter distributions of the photometric sample to those of the PS1-MDS spectroscopic sample and a larger literature spectroscopic sample, we find that these samples are consistent overall, but that the photometric sample extends to slower spins and lower ejecta masses, which correspond to lower-luminosity events, as expected for photometric selection. While our PS1-MDS photometric sample is still smaller than the overall SLSN spectroscopic sample, our methodology paves the way for an orders-of-magnitude increase in the SLSN sample in the LSST era through photometric selection and study.

Unified Astronomy Thesaurus concepts: Supernovae (1668)

1. Introduction

Hydrogen-poor (Type I) superluminous supernovae (SLSNe) are a rare subclass of core-collapse supernovae (CCSNe) that radiate ∼10–100 times more energy in the UV/optical than typical CCSNe, and generally exhibit longer durations and hotter continuum spectra (e.g., Chomiuk et al. 2011; Quimby et al. 2011; Nicholl et al. 2015; Inserra et al. 2017; De Cia et al. 2018; Lunnan et al. 2018). SLSNe account for only ∼0.1% of the volumetric CCSN rate (Quimby et al. 2018; Frohmaier et al. 2021), but in magnitude-limited optical surveys they account for ∼2% of all transients (Perley et al. 2020; Gomez et al. 2021), thanks to their high luminosity. SLSNe are classified spectroscopically based on the lack of hydrogen Balmer lines, the presence of a blue continuum, and unique early-time "W"-shaped O II absorption lines at ∼3600–4600 Å (e.g., Lunnan et al. 2013; Mazzali et al. 2016; Quimby et al. 2018; Nicholl 2021).

Several mechanisms have been proposed as powering SLSNe, but a magnetar central engine model (Kasen & Bildsten 2010; Woosley 2010; Dessart et al. 2012; Metzger et al. 2015; Nicholl et al. 2017b) has had the most success in explaining both the light curves and spectra of the SLSN population. This model accounts for the broad range of peak luminosities and timescales (e.g., Nicholl et al. 2017b; Blanchard et al. 2020), for the early UV/optical spectra (e.g., Nicholl et al. 2017a), for the nebular phase spectra (e.g., Nicholl et al. 2016b; Jerkstrand et al. 2017; Nicholl et al. 2019), and for the power-law decline rates observed in SN 2015bn and SN 2016inl at $\gtrsim 10^3$ day (Nicholl et al. 2018; Blanchard et al. 2021). Additional support for a magnetar engine comes from the low-metallicity host galaxies of SLSNe, which most closely resemble the hosts of long-duration gamma-ray bursts, another rare population of CCSNe that are likely powered by a central engine (Lunnan et al. 2014; Perley et al. 2016). While the magnetar engine model can explain the plethora of SLSN properties, other mechanisms have also been proposed to explain some SLSN properties; for example, Chen et al. (2022) recently argued that the light curves of at least some SLSNe from the Zwicky Transient Facility (Bellm et al. 2019) can be explained equally well with a combination of circumstellar (CSM) interaction and Ni^{51} decay. Furthermore, Hosseinzadeh et al. (2022) have also explored ejecta–CSM interaction as a potential source for postpeak undulations in SLSN light curves.

With ongoing and upcoming wide-field optical surveys, including in particular the Vera C. Rubin Observatory Legacy Survey of Space and Time (LSST; Ivezić et al. 2019), only a small fraction of SNe are being classified spectroscopically (∼10% currently, with ∼0.1% anticipated for LSST; Villar et al. 2020). This impacts the ability to advance the study of rare SN classes, such as SLSNe, in particular. As shown by Villar et al. (2018), LSST may yield $\sim 10^4$ SLSNe per year to $z \sim 3$ (of which at least ∼20% will have well-measured physical properties), but identifying these events requires *photometric* classification.

Recently, we presented two machine-learning-based SN photometric classification pipelines, `SuperRAENN` (Villar et al. 2020) and `Superphot` (Hosseinzadeh et al. 2020), trained on

Table 1
Sequential Selection Criteria

Metric (Applied Sequentially)	SuperRAENN	Superphot	Both Algorithms	Total SLSNe Classified[a]
No criteria applied	37	58	28	67
Not within 1″ of the AGN host center	25	44	16	53
Classification confidence $\geqslant 0.5$	18	28	10	36
$\geqslant 11$ detections across all four bands	16	17	9	24
PSRF $\leqslant 1.1$	13	13	7	19

Note.
[a] The total number of photometrically classified SLSNe takes into account the events classified by both algorithms.

2315 SN-like transients from the Pan-STARRS1 Medium Deep Survey (PS1-MDS; Huber et al. 2017). Both classifiers use multiple SN classes, including SLSNe, in particular. `SuperRAENN` combines a novel unsupervised recurrent autoencoder neural network (RAENN) with a random forest classifier for a semisupervised algorithm. `Superphot` utilizes a random forest approach, based on flexible analytic model fits to the light curves and their resulting parameters.

Here, as a demonstration of the type of approach and analysis that will be essential in the LSST era, we explore and study, for the first time, the *photometrically classified* SLSNe from PS1-MDS (Huber et al. 2017), as identified by `SuperRAENN` and `Superphot`. We first explore how to effectively construct a pure and well-measured subset of SLSNe from a photometrically classified sample (Section 2). We then model the light curves of the photometrically classified SLSNe with the same magnetar engine model that was previously used to study spectroscopically classified SLSNe (using `MOSFiT`; Guillochon et al. 2018; Section 3). Finally, we compare the resulting parameter distributions to those of the spectroscopically classified PS1-MDS SLSNe, as well as to the overall sample of spectroscopically classified SLSNe (Section 4).

Throughout the paper, we assume a flat ΛCDM cosmology, with $\Omega_{\rm m} = 0.308$ and $H_0 = 67.8\,{\rm km\,s^{-1}}$ Mpc, based on the Planck 2015 results (Planck Collaboration et al. 2016). We correct all photometry for Milky Way extinction using Schlafly & Finkbeiner (2011), and we follow the extinction law of Fitzpatrick (1999), with $R_V = 3.1$.

2. Sample Construction

The data used in this paper are from PS1-MDS. We refer the reader to Chambers et al. (2016) for details of the PS1 survey telescope and the PS1-MDS observing strategy, and to Villar et al. (2020) and Hosseinzadeh et al. (2020) for the definition of the overall sample of SN-like transients and their light curves, the description of the subsample of spectroscopically classified events, the photometric classification approaches and results, all the relevant data (including photometry and host galaxy redshifts), and complete descriptions of the algorithms and training processes.

In this paper, we focus on the sample of photometrically classified SLSNe.[7] Using `SuperRAENN` (Villar et al. 2020) and `Superphot` (Villar et al. 2018; Hosseinzadeh et al. 2020), we photometrically classified 58 and 37 SLSNe, respectively, using the same training set of 557 spectroscopically classified SNe, which includes 17 SLSNe that were studied in Lunnan et al. (2018). Here, we adopt the class with the highest probability as the predicted SN type for each transient.

Combining all the transients classified by the two algorithms as SLSNe, and accounting for 28 that are classified as SLSNe by both, we obtain an initial sample with 67 photometrically classified SLSNe. To further evaluate and potentially cull the photometric sample, we investigate several post-classification selection criteria. We find three effective criteria that help to reduce the sample contamination and lead to events with sufficient data to enable robust modeling. Furthermore, we apply an additional post-modeling quality cut, based on model convergence. The criteria and their effects on the sample size are summarized in Table 1, and we discuss them in detail below.

2.1. Active Galactic Nuclei Host Galaxies

Prior to applying our algorithms to the sample of PS1-MDS SN-like transients, we systematically excluded light curves with long-term variability to avoid contamination from active galactic nuclei (AGNs). Still, some large AGN flares with little other variability over the 4.5 yr time span of the survey could survive this preliminary qualitative cut and eventually be classified as SLSNe. In particular, Hosseinzadeh et al. (2020) find that 14 photometrically classified SLSNe with host galaxy spectra that exhibit broad AGN lines are located within 1″ of the host center.[8] While these could in principle be SLSNe located indistinguishably close to an AGN, they are more likely large AGN flares or tidal disruption events, neither of which are classification categories in `SuperRAENN` or `Superphot`. Eliminating these events results in a combined sample of 53 events (Table 1, row 2).

2.2. Classification Confidence

Our initial sample requires that the highest classification probability be assigned as SLSN. However, given the number of classification categories, this does not necessarily mean that the classification confidence is high. Hosseinzadeh et al. (2020) and Villar et al. (2020) show that increasing the classification confidence threshold to $p \gtrsim 0.75$ leads to higher purity[9] across the full range of classes, at the expense of sample completeness. Here, we apply a classification confidence threshold of $p_{\rm SLSN} \geqslant 0.5$ as a compromise between purity and sample size

[7] Both classification pipelines are open source and available via GitHub: https://github.com/villrv/SuperRAENN and https://github.com/griffin-h/superphot.

[8] These transients are PSc000478, PSc010120, PSc010186, PSc020026, PSc030013, PSc052281, PSc110163, PSc130394, PSc130732, PSc350614, PSc390545, PSc400050, PSc480585, and PSc550061.

[9] "Purity" refers to the fraction of a given photometric class that belongs to the equivalent spectroscopic class (Hosseinzadeh et al. 2020).

(which corresponds to a purity of ≈0.78; see Hosseinzadeh et al. 2020). This selection cut reduces the sample size from 53 to 36 events (Table 1, row 3).

2.3. Number of Light-curve Data Points

Both the classification confidence and the ability to meaningfully model the light curves with MOSFiT (Section 3.1) are affected by the number of light-curve data points; namely, the number of data points relates to the ability to constrain the MOSFiT models and return statistically meaningful posterior distributions. Here, we set a threshold of ⩾11 data points in total across the four observed filters (*griz*) to match the number of the model's free parameters.[10] This selection cut reduces the sample size from 36 to 24 (Table 1, row 4).

2.4. Model Convergence

The aforementioned selection criteria are applied prior to modeling. After all three criteria are applied, we model the 24 photometrically classified SLSNe with a magnetar central engine model, implemented in MOSFiT. Although we have reduced our sample to identify only events with a sufficient number of data points and high confidence as being SLSNe, light curves with marginal detections or potentially misclassified events could in principle survive the above pre-modeling selection metrics. Therefore, we include an additional cut based on the model convergence factor, as measured by calculating the Gelman–Rubin statistics, or the potential scale reduction factor (PSRF; Gelman & Rubin 1992), which estimates the extent to which the full parameter space has been explored in our Markov Chain Monte Carlo (MCMC) models. Brooks & Gelman (1998) suggest that a PSRF < 1.2 provides reliable convergence, but we set a stricter threshold of PSRF < 1.1, as done in Nicholl et al. (2017b) and Hsu et al. (2021), which is also the termination value for our models (see Section 3.1). This post-modeling selection cut reduces our sample size from 24 to 19 (Table 1, row 5).

Our final photometric sample consists of 10 events classified as SLSNe by both algorithms, with the remaining nine being classified as SLSN by either SuperRAENN or Superphot. See Table 2 for the predicted SN type of each transient in our final sample and their respective classification confidence.

2.5. Justification of Our Choices

In Figure 1, we show the combined effects on the final sample size of varying the minimum classification confidence and the number of data points; we use this as a guide, such that our final sample consists of events with sufficient confidence levels and data points to obtain a robust model. In each cell, we show the number of events that survive each pair of minimum thresholds for confidence and number of detections, and we quote the final sample size after applying both the AGN and convergence cuts in parentheses. To extract a sample size comparable to the PS1-MDS spectroscopic sample (17 events) that will return statistically meaningful results, we outline in Figure 1 the combinations of minimum confidence and detection thresholds that produce a minimal final sample size ⩾17. We find that our choices of the minimum confidence (⩾0.5) and the number of detections (⩾11) fall within the outlined region, indicating that our selection criteria are reasonable and justified.

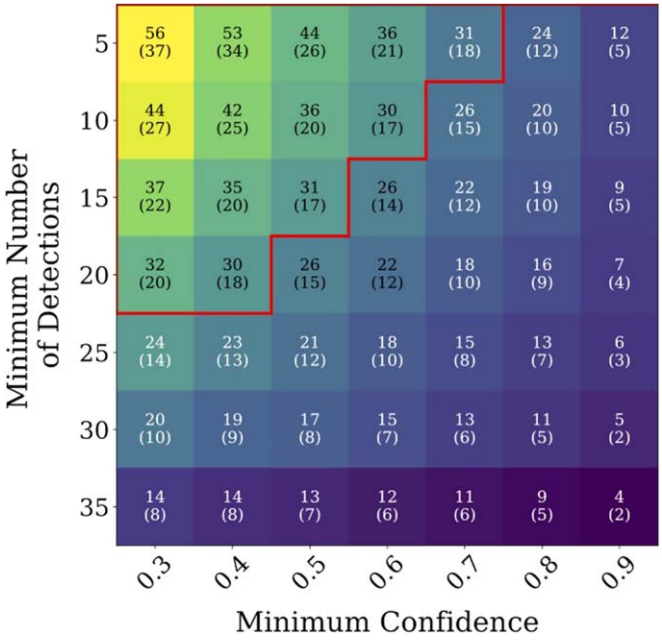

Figure 1. Matrix showing the effect of varying the minimum classification confidence and the minimum number of light-curve data points across all four filters. The top number in each cell indicates the total number of events (out of 67) satisfying both thresholds. The numbers in parentheses indicate the final sample size after removing AGN hosts and events with nonconverged models. The region outlined in red marks the boundary for combinations that result in a comparable sample size (⩾17) to the PS1-MDS spectroscopic sample.

Table 2
Classification Results for the Final SLSN Photometric Sample

	SuperRAENN		Superphot	
PScID	SN Type	Confidence	SN Type	Confidence
PSc000036	SLSN	1.00	SLSN	0.89
PSc000553[a]	SLSN	0.84	SNIIn	0.52
PSc061198	SLSN	0.41	SLSN	0.82
PSc070299	SLSN	1.00	SLSN	0.99
PSc080492[a]	SLSN	0.86	SNIIn	0.50
PSc091753[a]	SLSN	0.78	SNIIn	0.47
PSc110446	SLSN	0.94	SLSN	0.94
PSc120151[a]	SNIIn	0.66	SLSN	0.86
PSc130096[a]	SNIa	0.93	SLSN	0.71
PSc300035	SLSN	0.76	SLSN	0.89
PSc310006	SLSN	1.00	SLSN	0.98
PSc320338	SLSN	0.98	SLSN	0.94
PSc380044[a]	SNIIn	0.39	SLSN	0.58
PSc390461[a]	SNIa	1.00	SLSN	0.77
PSc390605[a]	SLSN	0.64	SNIIn	0.95
PSc420350	SLSN	0.39	SLSN	0.69
PSc450057[a]	SLSN	0.51	SNIIn	0.61
PSc480628	SLSN	0.61	SLSN	0.73
PSc490019	SLSN	0.60	SLSN	0.39

Note. The classification results for the final 19 photometric SLSNe from both SuperRAENN and Superphot. Here, we adopt the SN class with the highest classification probability as the predicted SN type for each transient. If either algorithm classifies an event as an SLSN, we include it in our sample.
[a] Event classified as an SLSN by only one classifier.

[10] One parameter is set to have a constant value, leaving us with 11 free parameters; see Section 3.1.

Table 3
Priors on the Magnetar Model Parameters

Parameter /Unit	Prior Shape	Lower Bound	Upper Bound	Gaussian	
				Mean	S.D.
P/ms	Flat	0.7	20	...	...
$B/10^{14}$ G	Flat	0.1	10	...	...
$M_{\rm ej}/M_{\odot}$	Flat	0.1	100	...	...
$v_{\rm ej}/10^4$ km s^{-1}	Gaussian	0.1	3.0	1.47	4.3
κ/ g cm^{-2}	Flat	0.05	0.2	...	...
κ_{γ}/ g cm^{-2}	Log-flat	0.01	100	...	...
$M_{\rm NS}/M_{\odot}$	Flat	1.4	2.2	...	...
$T_{\rm min}/10^3$ K	Gaussian	3.0	10.0	6.0	1.0
$n_{\rm H,host}$/cm^{-2}	Log-flat	10^{16}	10^{23}	...	...
$t_{\rm exp}$/days	Flat	−100	0	...	...
σ/mag	Log-flat	10^{-3}	100	...	...

Note. P is the initial spin period of the magnetar; B is the magnetic field strength; $M_{\rm ej}$ is the ejecta mass; $v_{\rm ej}$ is the ejecta velocity; κ is the opacity; κ_{γ} is the gamma-ray opacity; $M_{\rm NS}$ is the neutron star mass; $T_{\rm min}$ is the photospheric temperature floor; $n_{\rm H,host}$ is the hydrogen column density in the host galaxy, a proxy for extinction; $t_{\rm exp}$ is the time of explosion relative to the first observed data point; and σ is the additional photometric uncertainty required to yield a reduced chi-squared value of ≈1. All priors, including Gaussian priors, are bounded as specified above. For a detailed description of the model, see Nicholl et al. (2017b).

3. Magnetar Model Fits

3.1. Brief Description of the Model

We fit the optical light curves of the 19 photometrically classified SLSNe (selected as described in Section 2) using the Modular Open-Source Fitter for Transients (MOSFiT; Guillochon et al. 2018), with the magnetar spin-down model described in Nicholl et al. (2017b). MOSFiT is an open-source Python-based light-curve fitting package that employs an MCMC algorithm to fit a one-zone, gray-opacity analytical model to multiband light curves (Nicholl et al. 2017b).

The magnetar model has 12 free parameters, of which eight are nuisance parameters that we marginalize over, in order to obtain the four key physical parameters related to the ejecta and engine properties. We fix one of the nuisance parameters, the angle θ_{PB}, between the magnetic field and the rotational axis of the magnetar, to 90°, as this ensures that the derived B-field strength is a lower limit (following Nicholl et al. 2017b). The nuisance parameters, κ, κ_{γ}, $M_{\rm NS}$, and $n_{\rm H,host}$, are not well constrained by the model. Events with sufficient late-time observations may constrain the gamma-ray opacity κ_{γ}, but this is not the case for our sample. The neutron star mass is degenerate with the spin period and magnetic field strength, but is not well constrained. The explosion time, $t_{\rm exp}$, is the time between the explosion and the first observation in the pure magnetar model. The main parameters that constrain the observed properties of an SLSN are the neutron star's initial spin period, P; magnetic field strength, B; ejecta mass, $M_{\rm ej}$; and ejecta velocity, $v_{\rm ej}$ (the latter two can be combined to determine the kinetic energy, E_K). The model parameters and their priors are listed in Table 3.

For each light-curve fit, the first 10,000 iterations are used to burn in the ensemble, during which minimization is employed periodically, as the ensemble converges to the global optimum; the remainder of the run time is used to sample the posterior probability distribution. Convergence is measured by calculating the PSRF, and we terminate our fits when PSRF < 1.1. Most events typically require 30,000–60,000 iterations to reach convergence, depending on the number of data points and the scatter around our model.

3.2. Light-curve Fits

In Figure 2, we show the magnetar model light-curve fits for the 19 PS1-MDS photometrically classified SLSNe. The shaded regions are the MOSFiT light-curve fits, where the upper and lower bounds are the 1σ uncertainties calculated from the 120 MCMC walkers, while the solid light curves are based on the parameter medians. To allow for a proper comparison with the PS1-MDS spectroscopic sample, we also show in Figure 3 the 17 PS1-MDS spectroscopically classified SLSNe (which were used in the classification training samples). Previous studies (Nicholl et al. 2017b; Villar et al. 2018; Blanchard et al. 2020) have already modeled all but one of these events (PS1-12cil) in the same manner as this work. Two peculiar events from the PS1-MDS spectroscopically classified sample, PS1-11ap and PS1-12cil, exhibit postpeak undulations (e.g., Inserra et al. 2013; Nicholl et al. 2014, 2016a; Inserra et al. 2017; Hosseinzadeh et al. 2022). Since our MOSFiT model does not account for these "bumps," we replace the model of PS1-11ap from Blanchard et al. (2020) with the version presented in Hosseinzadeh et al. (2022), which converts these bumps into upper limits prior to fitting. We also include the model for PS1-12cil from Hosseinzadeh et al. (2022) to complete the PS1-MDS spectroscopic SLSN sample. For illustrative purposes, we extrapolate all light curves (both photometric and spectroscopic samples) back to the inferred explosion time and forward to 100 days after the last detection.

Overall, we find that the model fits the observed light curves well, and is better constrained for events with more extensive data. The resulting median values and 1σ uncertainties for the four main physical parameters (P, B, $M_{\rm ej}$, and $v_{\rm ej}$), calculated based on the posterior probability distributions from 120 MCMC walkers, are summarized in Table 4. Our model includes an intrinsic scatter term, σ, which attempts to model white systematic scatter not captured by our statistical uncertainties.

The sample median values and associated 1σ ranges of the four key model parameters, along with the kinetic energy,[11] $E_K = \frac{1}{2}M_{\rm ej}{v_{\rm ej}}^2$, for the PS1-MDS photometric and spectroscopic samples, are listed in Table 5. We also list in Table 5 the values for a larger SLSN compilation sample, which includes 82 spectroscopically classified SLSNe (81 from Hsu et al. 2021, plus PS1-12cil from Hosseinzadeh et al. 2022), as a comparison sample. Comparing these samples, we find that the PS1-MDS photometric sample displays somewhat slower spins, higher B-field values, and lower ejecta masses as compared to the other two samples. However, the values are in good agreement within the 1σ ranges.

4. Sample Properties

4.1. Observational Properties

The PS1-MDS samples (both spectroscopic and photometric) collectively span a wide range of redshifts, $z \approx 0.3$–2. To properly compare the observational properties of the

[11] Our model assumes the analytic density profile described in Margalit et al. (2018). For a homogeneous density profile, the kinetic energy is given by $E_K = \frac{3}{10}M_{\rm ej}{v_{\rm ej}}^2$.

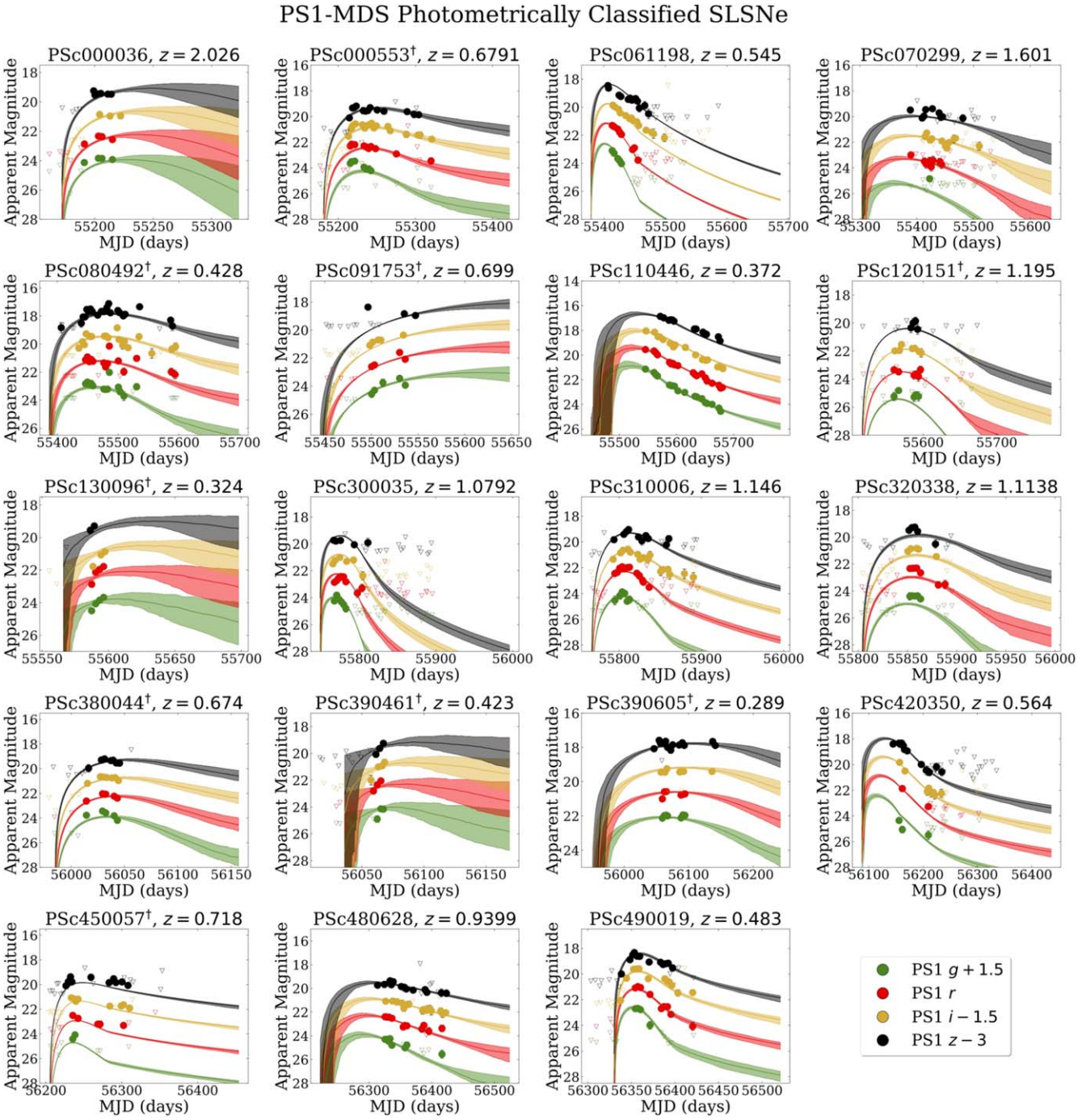

Figure 2. Multiband extinction-corrected apparent magnitude light curves of the 19 PS1-MDS photometrically classified SLSNe, along with our magnetar model fits using `MOSFiT`. The name of each transient and its spectroscopic host galaxy redshift are quoted at the top of each panel. The different filters are shifted for clarity, as indicated in the legend. Open triangles indicate 3σ upper limits, while solid circles indicate detections. The solid lines and shaded regions indicate the median model and 1σ ranges. Events classified as SLSNe by only one classifier are marked with daggers.

PS1-MDS SLSNe, we correct their observed peak apparent magnitudes to a single rest-frame filter. Since we do not have a complete set of spectra for the spectroscopic sample, and by definition have no spectra for the photometric sample, we do not apply a complete *K*-correction; instead, we apply only a cosmological *K*-correction factor of $2.5\log_{10}(1+z)$ to the peak magnitude in the band closest to the rest-frame *g* band for each event, and correct for Milky Way extinction. We plot the resulting peak *g*-band absolute magnitudes as a function of redshift in Figure 4. The PS1-MDS spectroscopic sample spans a range from ≈ -20.5 to ≈ -22.6, while the photometric sample spans a wider range from ≈ -18.7 to ≈ -22.6. As expected, lower-luminosity SLSNe are restricted to lower redshift ($z \lesssim 0.5$), while higher-luminosity events are distributed to higher redshift ($z \approx 2$). The spectroscopic sample is intrinsically more luminous, with a median peak magnitude of -22 as compared to -20.8 for the photometric sample.

We also plot in Figure 4 the per-visit PS1-MDS limiting magnitude of $\approx$23.3 (Villar et al. 2020), as well as the effective spectroscopic follow-up limit of $\approx$22.5 (Lunnan et al. 2018).

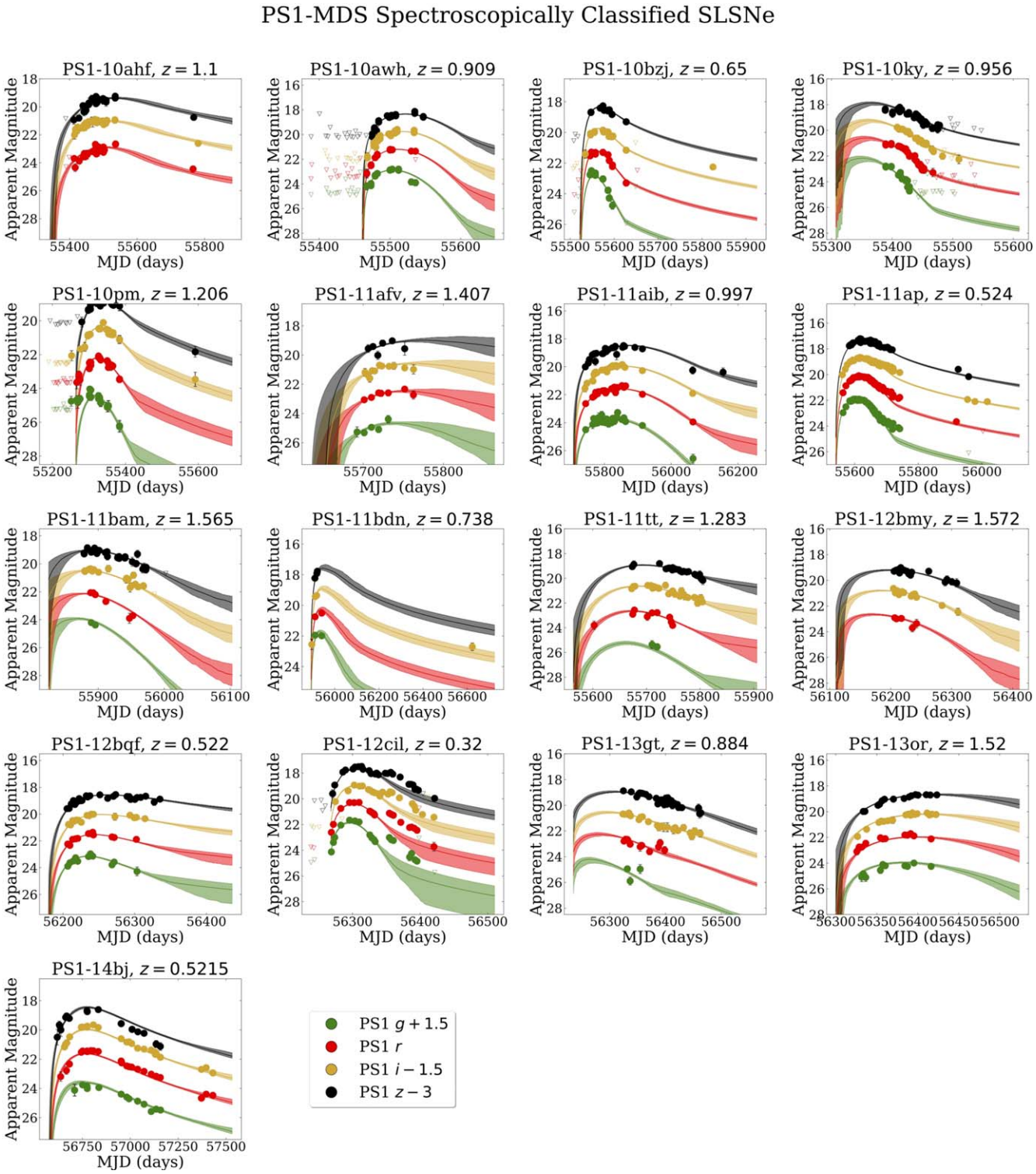

Figure 3. The same as Figure 2, but for the PS1-MDS spectroscopically classified SLSNe. The light curves for PS1-11ap and PS1-12cil are from Hosseinzadeh et al. (2022), modeled without the postpeak pumps.

The majority of the photometric sample have peak absolute magnitudes either around or below the spectroscopic follow-up depth, which explains why these events were not chosen for spectroscopic follow-up. However, there are five photometrically classified SLSNe (PSc061198, PSc080492, PSc110446, PSc390605, and PSc490019) at lower redshift ($z \leqslant 0.6$) that are more than 1 mag brighter than the threshold, but were not chosen as follow-up candidates.

4.2. Physical Properties and Correlations

In Figure 5, we show two-dimensional distributions of the primary physical parameters (P, B, $M_{\rm ej}$, and $v_{\rm ej}$; the medians of the posteriors) and redshifts of both the PS1-MDS sample and the SLSN compilation, which contains events from a wide range of surveys (including the PS1-MDS spectroscopic sample). We explore the differences between the three samples

Table 4
Median Magnetar Parameter Values for the Photometrically Classified SLSNe

SLSN Name	P (ms)	B (10^{14} G)	M_{ej} ($M_\odot$)	v_{ej} (10^3 km s^{-1})
PSc000036	$1.61^{+0.87}_{-0.58}$	$1.30^{+0.57}_{-0.42}$	$4.31^{+4.25}_{-2.16}$	$7.47^{+0.85}_{-1.64}$
PSc000553[a]	$7.45^{+0.97}_{-0.95}$	$1.56^{+0.67}_{-0.51}$	$3.19^{+1.87}_{-1.04}$	$6.83^{+0.96}_{-0.80}$
PSc061198	$6.89^{+0.82}_{-0.84}$	$4.73^{+0.91}_{-1.25}$	$1.69^{+0.46}_{-0.44}$	$11.46^{+0.46}_{-0.53}$
PSc070299	$2.32^{+1.81}_{-1.28}$	$1.87^{+1.00}_{-1.13}$	$9.38^{+15.07}_{-7.50}$	$5.91^{+1.12}_{-0.65}$
PSc080492[a]	$2.10^{+0.90}_{-0.69}$	$0.94^{+0.30}_{-0.29}$	$13.54^{+12.43}_{-4.75}$	$6.76^{+0.87}_{-0.74}$
PSc091753[a]	$2.18^{+0.83}_{-0.86}$	$0.27^{+0.23}_{-0.14}$	$28.62^{+37.64}_{-17.73}$	$3.97^{+0.21}_{-0.24}$
PSc110446	$2.27^{+1.07}_{-1.14}$	$1.40^{+0.78}_{-0.54}$	$7.52^{+19.93}_{-4.74}$	$8.22^{+1.98}_{-1.22}$
PSc120151[a]	$7.51^{+0.69}_{-0.93}$	$2.04^{+0.64}_{-0.49}$	$1.23^{+0.20}_{-0.23}$	$5.96^{+0.30}_{-0.38}$
PSc130096[a]	$5.30^{+4.18}_{-2.84}$	$1.55^{+2.20}_{-1.12}$	$25.45^{+30.36}_{-17.95}$	$3.00^{+1.12}_{-0.82}$
PSc300035	$2.87^{+1.16}_{-1.22}$	$7.66^{+1.36}_{-1.55}$	$1.75^{+0.33}_{-0.33}$	$14.09^{+1.47}_{-1.16}$
PSc310006	$4.35^{+0.66}_{-0.62}$	$0.97^{+0.41}_{-0.31}$	$1.44^{+0.38}_{-0.25}$	$11.99^{+1.08}_{-0.79}$
PSc320338	$6.02^{+1.06}_{-0.86}$	$1.46^{+0.67}_{-0.56}$	$1.93^{+0.47}_{-0.46}$	$8.63^{+1.36}_{-1.36}$
PSc380044[a]	$7.00^{+0.88}_{-0.95}$	$2.14^{+0.65}_{-0.52}$	$3.58^{+2.25}_{-1.44}$	$5.64^{+0.58}_{-0.64}$
PSc390461[a]	$1.53^{+0.85}_{-0.55}$	$0.08^{+0.07}_{-0.05}$	$47.89^{+28.57}_{-24.13}$	$4.60^{+0.57}_{-0.53}$
PSc390605[a]	$2.15^{+1.61}_{-0.94}$	$2.21^{+0.68}_{-0.67}$	$30.24^{+14.93}_{-10.10}$	$2.17^{+0.34}_{-0.22}$
PSc420350	$1.17^{+0.42}_{-0.29}$	$5.59^{+1.30}_{-1.27}$	$9.90^{+6.85}_{-2.60}$	$13.36^{+1.14}_{-1.26}$
PSc450057[a]	$10.83^{+1.03}_{-1.56}$	$2.31^{+0.42}_{-0.56}$	$1.16^{+0.84}_{-0.36}$	$9.02^{+0.26}_{-0.17}$
PSc480628	$4.67^{+0.71}_{-0.52}$	$1.74^{+0.36}_{-0.44}$	$2.74^{+1.97}_{-1.25}$	$3.71^{+0.89}_{-0.40}$
PSc490019	$7.98^{+1.07}_{-1.15}$	$5.95^{+0.91}_{-1.72}$	$1.50^{+0.65}_{-0.30}$	$10.74^{+1.34}_{-1.17}$

Note.
[a] Event classified as an SLSN by only one classifier.

Table 5
Magnetar Parameter Sample Median Values

Parameter	PS1-MDS Photometric	PS1-MDS Spectroscopic	SLSN Compilation
P (ms)	$4.35^{+3.11}_{-2.32}$	$1.96^{+2.36}_{-0.90}$	$2.67^{+3.26}_{-1.34}$
B (10^{14} G)	$1.56^{+3.28}_{-0.63}$	$0.88^{+1.43}_{-0.59}$	$1.14^{+1.75}_{-0.86}$
M_{ej} ($M_\odot$)	$3.19^{+22.6}_{-1.70}$	$7.70^{+16.5}_{-4.35}$	$4.56^{+6.02}_{-2.37}$
v_{ej} (10^3 km s)	$6.83^{+4.69}_{-2.89}$	$9.09^{+4.15}_{-3.10}$	$9.25^{+3.40}_{-2.58}$
E_K (10^{51} erg)	$2.21^{+2.98}_{-1.10}$	$6.48^{+7.93}_{-4.24}$	$3.78^{+5.09}_{-1.86}$

Note. The median values and 1σ ranges for the magnetar engine and ejecta parameters of the PS1-MDS SLSN samples (photometric and spectroscopic) and the SLSN compilation sample (from Hsu et al. 2021, with the addition of PS1-12cil), including the 17 PS1-MDS spectroscopically classified SLSNe.

and the parameter correlations for the combined sample (all three samples together, 101 SLSNe in total). Specifically, we compare the PS1-MDS photometric sample and the spectroscopic compilation sample using the two-sample Kolmogorov–Smirnov (K–S) test (Smirnov 1948) and the two-sample Anderson–Darling (A–D) test (Anderson & Darling 1952). Both tests are designed to determine whether two distributions arise from the same underlying population. The A–D test is a modification of the K–S test that is more sensitive to the tails of a distribution, whereas the K–S test gives more weight to the mean of a distribution. We report the resulting p-values from these tests, to determine if both are drawn from the same parameter distribution, at the top of each column in Figure 5.

The differences in the redshift distributions between the two samples reflect the design characteristics of the various surveys (e.g., PS1-MDS, Dark Energy Survey, Palomar Transient Factory, etc.). In terms of the magnetar model parameters, we find that the distributions are overall in good agreement, except for the ejecta velocity, which has statistically significant

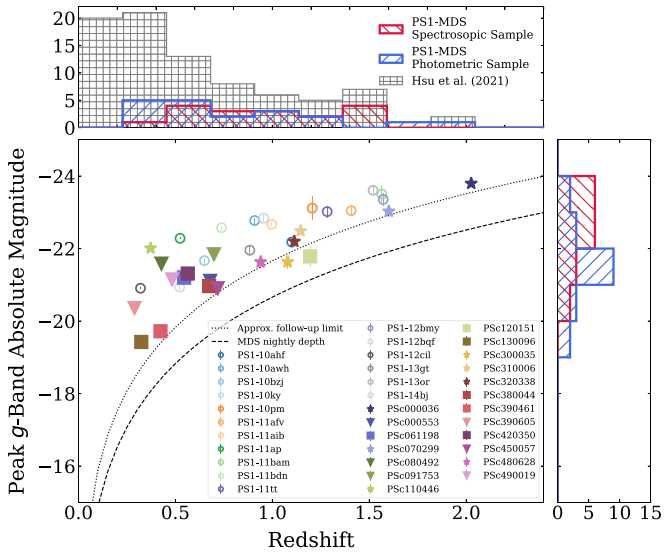

Figure 4. Peak absolute rest-frame g-band magnitude vs. redshift for the PS1-MDS SLSNe (solid squares: photometrically classified by `Superphot` only; solid triangles: photometrically classified by `SuperRAENN` only; solid stars: photometrically classified by both `SuperRAENN` and `Superphot`; open circles: spectroscopically classified). The top panel shows the redshift distribution of the PS1-MDS photometric (blue) and spectroscopic (red) samples compared to the SLSN compilation from Hsu et al. (2021) (82 spectroscopic SLSNe, including the 17 from PS1-MDS), while the right panel shows the distributions of the peak magnitudes for the PS1-MDS samples. Each peak magnitude is corrected for Galactic extinction and includes a cosmological K-correction factor of $2.5\log(1+z)$.

p-values for the A–D test. This indicates that we can reject the null hypothesis at 95% confidence that the ejecta velocity for the photometric and the spectroscopic compilation samples are drawn from the same distribution. This may be caused by the sensitivity of the A–D test to tail distributions. The spectroscopic compilation sample spans a range of $v_{ej} \approx (3.6\text{–}16) \times 10^3$ km s^{-1}, while the photometric sample spans a range of $v_{ej} \approx (2.2\text{–}14) \times 10^3$ km s^{-1}, with two events[12] (PSc130096 and PSc390605) having v_{ej} values that fall outside the range of the spectroscopic population. Removing these two outliers returns an updated A–D test p-value of ≈0.06, suggesting that other than these two specific data points, the remainder of the photometric sample fit into the spectroscopic sample well. We explore the posterior distributions of the magnetar parameters from the photometric sample in more detail in the next subsection.

As done in previous SLSN parameter studies (e.g., Blanchard et al. 2020; Hsu et al. 2021), we combine the PS1-MDS photometric and literature samples to confirm known correlations and explore new ones. For each pair of parameters, we perform a Monte Carlo procedure to calculate the Spearman rank correlation coefficient (ρ; Spearman 1904) and its associated 1σ bound, using the method described in Curran (2014). The results are summarized in each panel of Figure 5. We find the same results as in Hsu et al. (2021), where most parameter combinations exhibit either no correlation, mild correlations, or mild correlations that are primarily due to the absence of events in specific areas of the parameter space. The mass–spin correlation first discussed in Blanchard et al. (2020) remains strong after merging the photometric and

[12] The two v_{ej} outliers (PSc130096 and PSc390605) have relatively few data points. PSc130096 lacks a definitive peak and any postpeak data, and the model is therefore only marginally constrained. PSc390605 similarly lacks prepeak and postpeak data, again leading to a marginally constrained model.

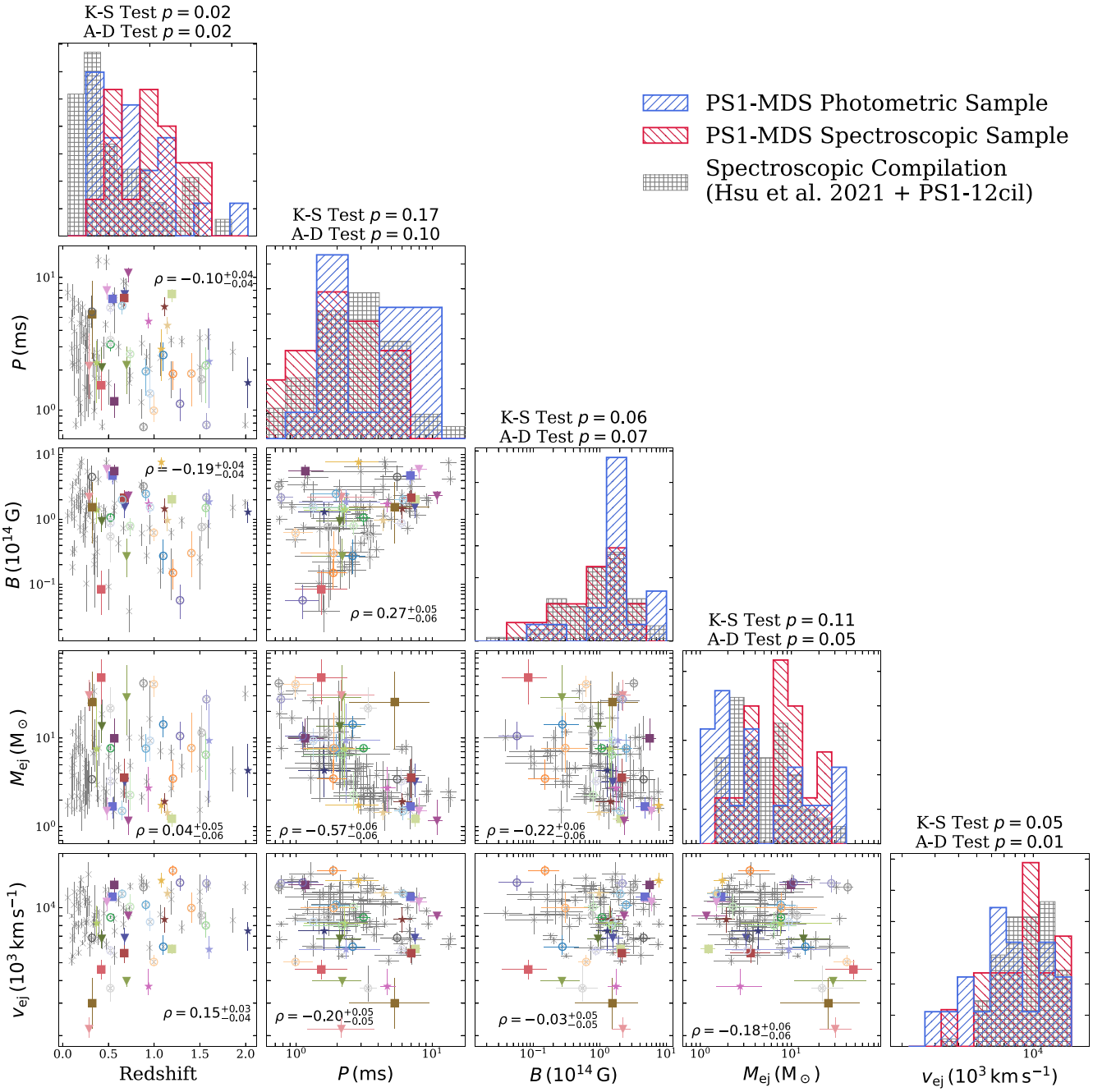

Figure 5. Median values and 1σ uncertainties of the key magnetar model parameters (P, B, M_{ej}, and v_{ej}; solid squares: photometric; open circles: spectroscopic; and the plot symbols for the photometrically classified SLSNe are the same as in Figure 4). The models for PS1-11ap and PS1-12cil are both obtained from Hosseinzadeh et al. (2022). The gray crosses mark the remaining spectroscopically confirmed SLSNe from Hsu et al. (2021). In the top panels, we show the parameter distributions for the PS1-MDS photometric sample (blue), the PS1-MDS spectroscopic sample (red), and the SLSN compilation sample (gray), along with the median p-values associated with both the K–S test and the A–D test statistics, calculated using the PS1-MDS photometric sample and the SLSN compilation. In each panel, we quote the median value and 1σ bound of the Spearman rank correlation coefficient, using the PS1-MDS photometric sample and literature data set. Of all the parameter pairs, P and M_{ej} exhibit the strongest correlation, consistent with the findings in Blanchard et al. (2020) and Hsu et al. (2021).

spectroscopic samples. All other mild correlations have been previously explained as being due to observational biases in Blanchard et al. (2020) and Hsu et al. (2021), and we do not find any new statistically significant correlations here.

4.3. Posterior Distributions of the Photometric Sample

To explore any differences in the magnetar and ejecta parameters between the PS1-MDS photometric and spectroscopic samples, we show in Figure 6 the joint posterior distributions of the PS1-MDS photometric, PS1-MDS spectroscopic, and compilation samples. We construct the joint posterior distributions by selecting 100 randomly sampled walkers from each `MOSFiT` fit.[13]

To capture the uncertainties in the test statistics, we calculate and report in each panel the two-sample K–S test and the

[13] We take 100 here instead of the full 120 walkers as described in Section 3.2 because some events modeled previously in Blanchard et al. (2020) only have 100 walkers.

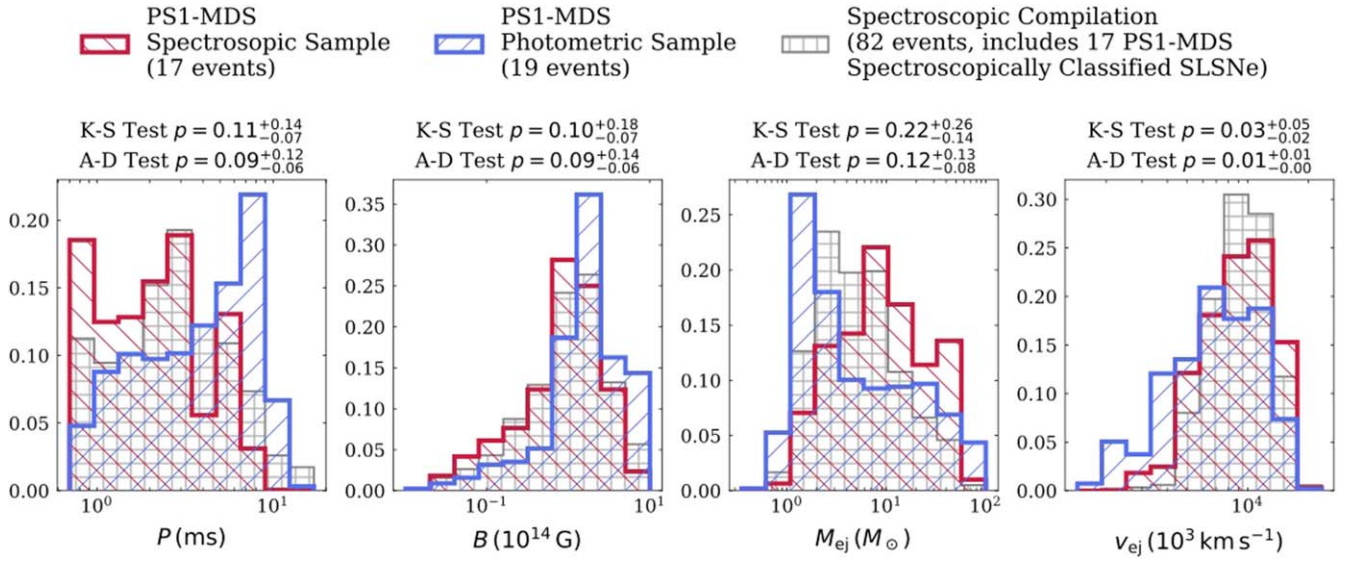

Figure 6. Normalized joint posterior distributions of the magnetar and ejecta parameters for the PS1-MDS photometric (blue), PS1-MDS spectroscopic (red), and spectroscopic compilation (gray) samples. The distributions are the summed posteriors of the `MOSFiT` parameters, consisting of 100 randomly sampled MCMC walkers from each SLSN fit. At the top of each panel, we quote the median p-values and their 1σ ranges from both the K–S and the A–D tests, using the bootstrap method, by comparing the PS1-MDS photometric sample and the SLSN compilation.

two-sample A–D test p-values between the PS1-MDS photometric sample and the spectroscopic compilation using a modified bootstrap method. For each parameter, we calculate a distribution of p-values by repeating the following procedure 5000 times. We assemble a joint posterior for the 19 photometrically classified SLSNe by randomly drawing one MCMC walker from the individual posterior for each event, and we do the same for the 82 spectroscopically classified SLSNe. We then calculate p-values for the K–S and A–D tests, comparing these two joint posteriors. We report the median and 1σ bounds of these distributions of the resulting p-values on top of each panel in Figure 6.

The posterior distributions for the physical parameters are in good agreement, except for v_{ej}, as noted previously; removing PSc130096 and PSc390605 from the photometric sample leads to $p = 0.11^{+0.15}_{-0.08}$ (K–S) and $p = 0.05^{+0.06}_{-0.03}$ (A–D). We also note that while the K–S and A–D tests indicate that the distributions of P and M_{ej} are drawn from the same distribution, the photometric sample skews to slower spins and lower ejecta masses (this trend is still in agreement with the mass–spin correlation). This difference can be ascribed to the systematically lower luminosities of the photometric SLSNe (Figure 4) compared to the PS1-MDS spectroscopic SLSNe.

4.4. Effects of Classification Uncertainty

As indicated in Table 2, nine of the 19 photometrically classified SLSNe in our final sample were designated as SLSNe by only one of the two classifiers. To investigate the impact of these cases of classification disagreement, we repeat the analyses in the previous subsections using only the events classified as SLSNe by both `Superphot` and `SuperRAENN`. This "consensus" photometric sample spans a peak absolute magnitude range from ≈ -20.3 to ≈ -22.6. However, despite excluding some of the lowest-luminosity events, the median peak magnitude is still ≈ 1 mag dimmer than that of the spectroscopic sample (see Figure 7, left), and we find the same trend of systematically lower luminosity at any redshift, as seen for the full sample in Figure 4. Our conclusion about the lower luminosities probed by the photometric sample thus remains unchanged.

Systematically removing objects classified as SLSNe by only one classifier eliminates the disagreement in the v_{ej} distributions, but introduces mildly statistically significant differences in B and M_{ej}. The consensus sample shifts to higher ranges of $B \approx (1\text{–}7.7) \times 10^{14}$ G, $v_{ej} \approx (0.37\text{–}1.41) \times 10^4$) km s^{-1}, a lower range of $M_{ej} \approx 1.4\text{–}9.9\ M_\odot$, and a similar range of $P \approx$ (1.17–7.98) ms in parameter distributions. These shifts are all consistent and expected for SLSNe with higher luminosities. See Figure 7 for these changes in the magnetar model parameters. The shift in B is reflected in the posterior distribution, but not as strongly in M_{ej}.

5. Discussion and Conclusions

In this paper, we have presented a case study for time-domain science with machine-learning-based photometric classification, focusing on SLSNe from PS1-MDS. Our analysis has consisted of two critical aspects that would need to be undertaken for any such future studies (for SLSNe or any other types of transients). First, we began with a sample of events nominally classified as SLSNe by two independent machine-learning-based pipelines (`SuperRAENN` and `Superphot`). We then applied various selection criteria to increase the sample purity (e.g., removing likely AGN flares and setting a higher minimum classification probability threshold), at the cost of sample completeness. Our sample size following these cuts was 36% of the initial sample (24 of 67). Subsequent to the sample refinement, we carried out modeling with `MOSFiT` to extract physical parameters in order to compare the photometric sample with existing spectroscopic samples modeled in the same way. The requirement for model convergence eliminated five additional events from the sample (a 21% reduction, from 24 to 19). These two critical steps of sample refinement and modeling will be essential for all studies with photometrically classified samples.

Comparing our photometric SLSN sample to the PS1-MDS spectroscopically classified SLSNe and to the larger sample of spectroscopic SLSNe, we find an overall similarity in both the

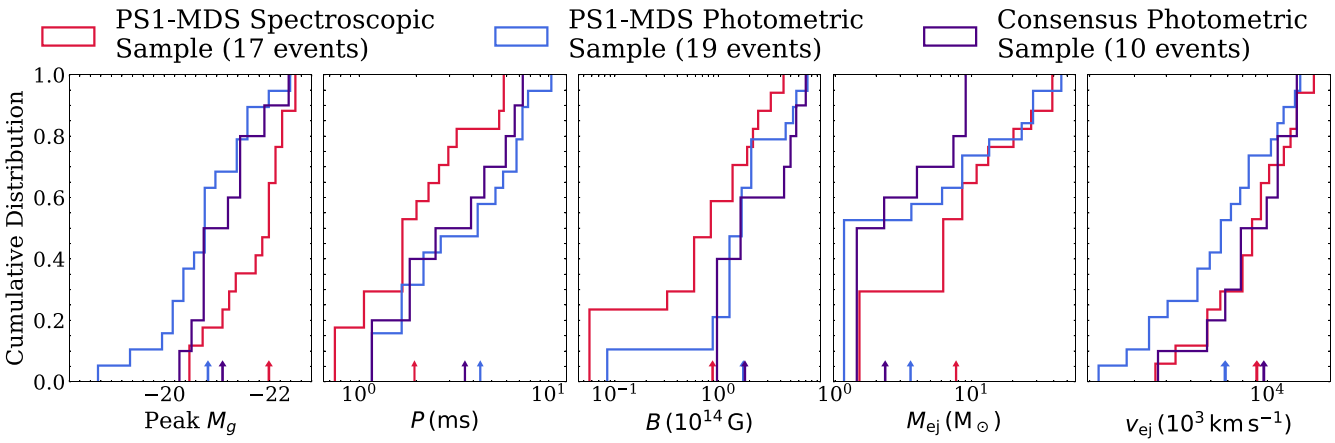

Figure 7. Cumulative distributions of the peak absolute rest-frame g-band magnitude and median magnetar model parameter values for the PS1-MDS spectroscopic (red), photometric (blue), and consensus photometric (purple) samples. The arrows in each panel indicate the median parameter value for the samples. The consensus photometric sample contains only events classified as SLSNe by both classifiers. It exhibits a higher median magnitude of ≈ -21.1 (purple arrow) compared to ≈ -20.8 for the full photometric sample, but is still ≈ 1 mag dimmer than the median of ≈ -22 for the spectroscopic sample. Even though the full and the consensus photometric samples have comparable median B values ($\approx 1.74 \times 10^{15}$ G and 1.80×10^{15} G for the full and consensus samples, respectively), the consensus sample spans a much narrower and higher range in B. The shift in M_{ej} is more strongly reflected, with a lower median value ($\approx 3.58\ M_\odot$, full; $\approx 2.33\ M_\odot$, consensus) at a lower range. All of the shifts in the magnetar model parameters are consistent with SLSNe having higher luminosities than in the full photometric sample.

observed properties and the inferred magnetar and ejecta parameters. We do note a potential shift in the photometric sample to slower magnetar spins and lower ejecta masses, which may reflect the fact that the photometric SLSNe are systematically dimmer than the spectroscopic PS1-MDS SLSNe (due to the shallower effective magnitude limit required for spectroscopy). If this is indeed the case, then it highlights an important advantage of photometric classification in deep surveys (such as PS1-MDS and LSST).

Our initial classifications and subsequent modeling both rely on the existence of redshift information. In the case of our PS1-MDS sample, the redshifts were determined from host galaxy spectroscopy after the survey had concluded. Such data may be difficult to obtain for the large samples expected from LSST (e.g., $\gtrsim 10^6$ SNe per year and $\sim 10^4$ SLSNe per year; Villar et al. 2018). However, robust photometric redshifts are likely to be as useful as spectroscopic redshifts. We also note that one source of contamination in our initial photometric sample appears to be AGNs (21%, 14 of 67 events), despite the fact that the PS1-MDS sample was designed to eliminate variable AGNs. These contaminating AGNs were again identified via host galaxy spectroscopy, which will not be available for the LSST samples; a more robust elimination of AGN will be essential.

Overall, our analysis highlights some challenges in constructing pure samples of photometrically classified SNe, but we believe that these challenges are surmountable. The photometric sample explored here is smaller than the overall known spectroscopic sample by a factor of several, but, looking forward to LSST, even a highly conservative selection with relatively low completeness will easily exceed the spectroscopic sample by two orders of magnitude.

The Berger Time Domain group at Harvard is supported in part by NSF and NASA grants, including support by the NSF under grant AST-2108531, as well as by the NSF under Cooperative Agreement PHY-2019786 (The NSFAI Institute for Artificial Intelligence and Fundamental Interactions http://iafi.org/). V.A.V. acknowledges support in part from the NSF through grant AST-2108676. The computations presented in this work were performed on the FASRC Cannon cluster supported by the FAS Division of Science Research Computing Group at Harvard University.

Software: Astropy (Astropy Collaboration et al. 2013, 2018), extinction (Barbary 2016), `MOSFiT` (Guillochon et al. 2018), Matplotlib (Hunter 2007), NumPy (Oliphant 2006), pymccorrelation (Curran 2014; Privon et al. 2020), Scipy (Virtanen et al. 2020), `Superphot` (Hosseinzadeh et al. 2020), `SuperRAENN` (Villar et al. 2020).

Facility: ADS, PS1.

ORCID iDs

Brian Hsu https://orcid.org/0000-0002-9454-1742
Griffin Hosseinzadeh https://orcid.org/0000-0002-0832-2974
V. Ashley Villar https://orcid.org/0000-0002-5814-4061
Edo Berger https://orcid.org/0000-0002-9392-9681

References

Anderson, T. W., & Darling, D. A. 1952, Ann. Math. Stat., 23, 193
Astropy Collaboration, Price-Whelan, A. M., Sipőcz, B. M., et al. 2018, AJ, 156, 123
Astropy Collaboration, Robitaille, T. P., Tollerud, E. J., et al. 2013, A&A, 558, A33
Barbary, K. 2016, JOSS, 1, 58
Bellm, E. C., Kulkarni, S. R., Barlow, T., et al. 2019, PASP, 131, 068003
Blanchard, P. K., Berger, E., Nicholl, M., et al. 2021, ApJ, 921, 64
Blanchard, P. K., Berger, E., Nicholl, M., & Villar, V. A. 2020, ApJ, 897, 114
Brooks, S. P., & Gelman, A. 1998, J. Comput. Graph. Stat., 7, 434
Chambers, K. C., Magnier, E. A., Metcalfe, N., et al. 2016, arXiv:1612.05560
Chen, Z. H., Yan, L., Kangas, T., et al. 2022, arXiv:2202.02060
Chomiuk, L., Chornock, R., Soderberg, A. M., et al. 2011, ApJ, 743, 114
Curran, P. A. 2014, arXiv:1411.3816
De Cia, A., Gal-Yam, A., Rubin, A., et al. 2018, ApJ, 860, 100
Dessart, L., Hillier, D. J., Waldman, R., Livne, E., & Blondin, S. 2012, MNRAS, 426, L76
Fitzpatrick, E. L. 1999, PASP, 111, 63
Frohmaier, C., Angus, C. R., Vincenzi, M., et al. 2021, MNRAS, 500, 5142
Gelman, A., & Rubin, D. B. 1992, StaSc, 7, 457
Gomez, S., Berger, E., Hosseinzadeh, G., et al. 2021, ApJ, 913, 143
Guillochon, J., Nicholl, M., Villar, V. A., et al. 2018, ApJS, 236, 6
Hosseinzadeh, G., Berger, E., Metzger, B. D., et al. 2022, ApJ, 933, 14
Hosseinzadeh, G., Dauphin, F., Villar, V. A., et al. 2020, ApJ, 905, 93

Hsu, B., Hosseinzadeh, G., & Berger, E. 2021, ApJ, 921, 180
Huber, M. & PS1 Science Consortium, & Pan-STARRS IPP Team 2017, AAS Meeting, 229, 237.06
Hunter, J. D. 2007, CSE, 9, 90
Inserra, C., Nicholl, M., Chen, T. W., et al. 2017, MNRAS, 468, 4642
Inserra, C., Smartt, S. J., Jerkstrand, A., et al. 2013, ApJ, 770, 128
Ivezić, Ž., Kahn, S. M., Tyson, J. A., et al. 2019, ApJ, 873, 111
Jerkstrand, A., Smartt, S. J., Inserra, C., et al. 2017, ApJ, 835, 13
Kasen, D., & Bildsten, L. 2010, ApJ, 717, 245
Lunnan, R., Chornock, R., Berger, E., et al. 2013, ApJ, 771, 97
Lunnan, R., Chornock, R., Berger, E., et al. 2014, ApJ, 787, 138
Lunnan, R., Chornock, R., Berger, E., et al. 2018, ApJ, 852, 81
Margalit, B., Metzger, B. D., Thompson, T. A., Nicholl, M., & Sukhbold, T. 2018, MNRAS, 475, 2659
Mazzali, P. A., Sullivan, M., Pian, E., Greiner, J., & Kann, D. A. 2016, MNRAS, 458, 3455
Metzger, B. D., Margalit, B., Kasen, D., & Quataert, E. 2015, MNRAS, 454, 3311
Nicholl, M. 2021, A&G, 62, 5.34
Nicholl, M., Berger, E., Blanchard, P. K., Gomez, S., & Chornock, R. 2019, ApJ, 871, 102
Nicholl, M., Berger, E., Margutti, R., et al. 2016b, ApJL, 828, L18
Nicholl, M., Berger, E., Margutti, R., et al. 2017a, ApJL, 835, L8
Nicholl, M., Berger, E., Smartt, S. J., et al. 2016a, ApJ, 826, 39
Nicholl, M., Blanchard, P. K., Berger, E., et al. 2018, ApJL, 866, L24
Nicholl, M., Guillochon, J., & Berger, E. 2017b, ApJ, 850, 55
Nicholl, M., Smartt, S. J., Jerkstrand, A., et al. 2014, MNRAS, 444, 2096
Nicholl, M., Smartt, S. J., Jerkstrand, A., et al. 2015, MNRAS, 452, 3869
Oliphant, T. E. 2006, A Guide to NumPy (USA: Trelgol Publishing)
Perley, D. A., Fremling, C., Sollerman, J., et al. 2020, ApJ, 904, 35
Perley, D. A., Quimby, R. M., Yan, L., et al. 2016, ApJ, 830, 13
Planck Collaboration, Ade, P. A. R., Aghanim, N., et al. 2016, A&A, 594, A13
Privon, G. C., Ricci, C., Aalto, S., et al. 2020, ApJ, 893, 149
Quimby, R. M., De Cia, A., Gal-Yam, A., et al. 2018, ApJ, 855, 2
Quimby, R. M., Kulkarni, S. R., Kasliwal, M. M., et al. 2011, Natur, 474, 487
Schlafly, E. F., & Finkbeiner, D. P. 2011, ApJ, 737, 103
Smirnov, N. 1948, Ann. Math. Stat., 19, 279
Spearman, C. 1904, AJP, 15, 72
Villar, V. A., Hosseinzadeh, G., Berger, E., et al. 2020, ApJ, 905, 94
Villar, V. A., Nicholl, M., & Berger, E. 2018, ApJ, 869, 166
Virtanen, P., Gommers, R., Oliphant, T. E., et al. 2020, NatMe, 17, 261
Woosley, S. E. 2010, ApJL, 719, L204